

pubs.acs.org/JPCB Article

Expulsion of Hydroxide Ions from Methyl Hydration Shells

Aria J. Bredt, Yongbin Kim, Denilson Mendes de Oliveira, Andres S. Urbina, Lyudmila V. Slipchenko, and Dor Ben-Amotz*



Cite This: J. Phys. Chem. B 2022, 126, 869-877



ACCESS

Metrics & More

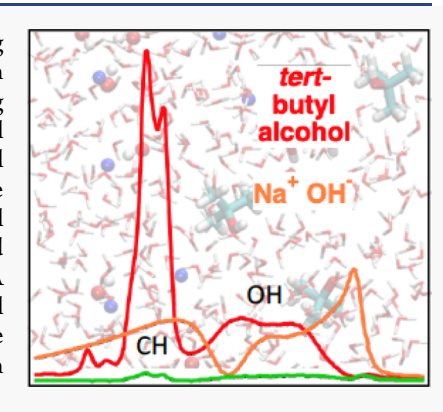


Article Recommendations



Supporting Information

ABSTRACT: The affinity of hydroxide ions for methyl hydration shells is assessed using a combined experimental and theoretical analysis of tert-butyl alcohol (TBA) dissolved in pure water and aqueous NaOH and NaI. The experimental results are obtained using Raman multivariate curve resolution (Raman-MCR) and a new three-component total least squares (Raman-TLS) spectral decomposition strategy used to highlight vibrational perturbations resulting from interactions between TBA and aqueous ions. The experiments are interpreted and extended with the aid of effective fragment potential molecular dynamics (EFP-MD) simulations, as well as Kirkwood-Buff calculations and octanol/water partition measurements, to relate TBA-ion distribution functions to TBA solubility changes. The combined experimental and simulation results reveal that methyl group hydration shells more strongly expel hydroxide than iodide anions, whose populations near the methyl groups of TBA are predicted to be correlated with sodium counterion localization near the TBA hydroxyl group.



■ INTRODUCTION

Although aqueous ions are generally expected to shun nonpolar interfaces (due to their lower dielectric constant), the partitioning of hydroxide ions to such interfaces remains a subject of debate. For example, the electrophoretic mobility of oil and air droplets in water has been interpreted by some authors as implying up to about a million-fold enhancement of the OH⁻ concentration at nonpolar air-water and oil-water interfaces.^{1,2} However, other experiments, including surface tension and surface-selective nonlinear optical measurements,³ as well as classical and quantum simulations, find much smaller OH adsorption, although the predicted degree to which OH is attracted or repelled from macroscopic nonpolar interfaces and molecular hydration shells has not yet been definitively established.3-15 Additional experimental measurements of the influence of aqueous ions on molecular solubilities and protein folding suggest a close connection between the affinity of ions for macroscopic air-water and molecular hydration-shell interfaces containing nonpolar groups, providing further evidence that OH is expelled from such interfaces. 16-18 More generally, Kirkwood-Buff theory provides a fundamental connection between molecular solubility and the local depletion (or accumulation) of ions in the solute's hydration shell. 19-21 Here, we revisit these issues, and particularly the affinity of OH- for methylated interfaces, by performing Raman multivariate curve resolution (Raman-MCR) and total least squares (Raman-TLS) decompositions of the vibrational spectra of aqueous solutions containing tert-butyl alcohol (TBA) and either NaOH or NaI. Our experimental results, interpreted and extended with the aid of effective fragment potential molecular dynamic (EFP-MD), reveal that the three

methyl groups of TBA more strongly exclude OH- than I-. Additional confirmation of the latter conclusion is obtained using Kirkwood-Buff theory to link TBA-ion distribution functions and TBA solubility, 19 implemented using both experimental TBA solubility measurements and EFP-MD distribution function predictions.

METHODS

Experimental Raman Measurement Methods. tert-Butyl alcohol (Sigma-Aldrich, ≥99.7%), sodium iodide (Sigma-Aldrich, ≥99.5%), and sodium hydroxide (Acros Organics, 98.5%) were used to prepare aqueous solutions. First, the salt and the TBA were weighed into individual 10 mL volumetric flasks and diluted to 1 and 0.5 M, respectively, with water from a Millipore purification system (H_2O , 18.2 $M\Omega$ cm from Milli-Q UF plus). Then, TBA was weighed into a 5 mL volumetric flask and diluted with the aqueous salt solution from the previous step to obtain a 0.5 M solution of TBA in the aqueous salt solvent. Each volumetric flask was inverted several times to ensure all solids were dissolved and the resulting equilibrated solutions were pipetted into 1 cm glass cuvettes and capped. All glassware and cuvettes were previously washed and dried in an oven overnight. All samples

Received: September 24, 2021 Revised: November 26, 2021 Published: January 25, 2022





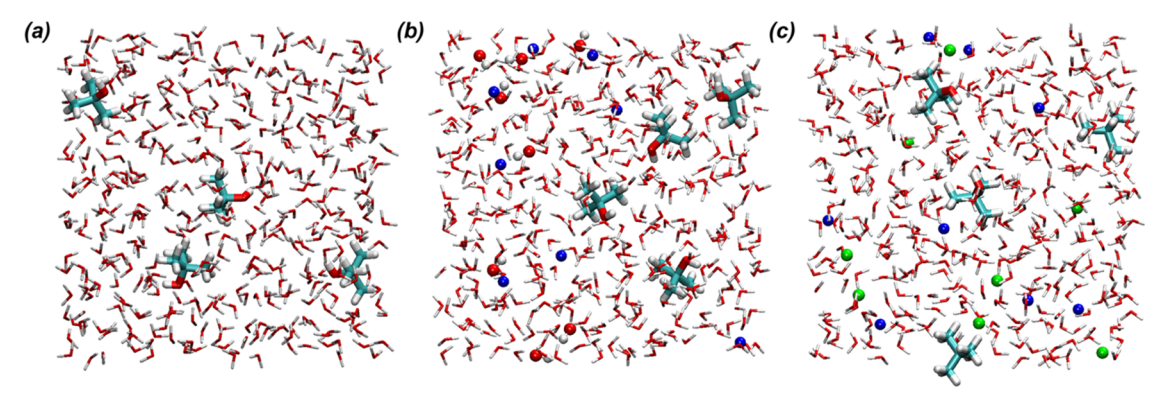


Figure 1. Snapshots of (a) TBA-water, (b) TBA-water-NaOH, and (c) TBA-water-NaI systems. The Na^+ ions are represented by blue spheres, OH^- is shown with red and white spheres, and I^- is shown with green spheres.

were freshly prepared, and Raman spectra were collected within 24 h (or after longer equilibration, in the case of the two-phase partitioning measurements described below).

The Raman spectra were collected using a home-built optical system with a 514.45 nm (~20 mW power at the sample) Ar-ion laser, 300 mm focal length spectrograph (SpectraPro300i, Acton Research Inc.), with a 300 grooves/mm grating, ~50 mm slit width, a thermoelectrically cooled charge-coupled device (CCD) camera (Princeton Instruments Inc., Pixis 400B), and fiber bundle collection optics, as previously described. The sample temperature was regulated to 20.0 °C using a temperature-controlled cell holder (Quantum Northwest). ²³

Multivariate curve resolution (Raman-MCR)²⁴ was implemented using the self-modeling curve resolution (SMCR) algorithm, 25 to obtain solute-correlated (SC) spectra containing spectral features from both the solute and perturbed solvent molecules. 24,26-29 To more sensitively uncover spectral features arising from ion-induced perturbation of TBA CH and CC stretch bands, the solution spectra were fit to a linear combination of pure water (W) and the first-round of SC spectra of TBA (SC_{TBA}) in water and the salt in water (SC_{salt}), using the following three-component total least squares (Raman-TLS) analysis strategy. Specifically, the Raman-TLS analysis begins by performing a subpixel shift of all of the spectra to precisely register their frequency axes (as previously described), 23,30 followed by performing a TLS fit of the measured spectra to the W, SC_{TBA} , and SC_{salt} spectra. The coefficients of the three components are then manually adjusted to obtain a non-negative minimum-area residual spectrum, equal to the difference between the measured mixture spectrum and the sum of the three-component spectra, in which all of the TLS residual bands have minimum areas and positive intensities above the local baseline. The baseline is fit to a quadratic function over a frequency range of 600-4000 cm⁻¹ at manually selected baseline points spanning that spectral region. In practice, we found that it is convenient to first slightly adjust the TBA SC coefficient to obtain minimumarea non-negative CC and CH bands and then slightly adjust the pure water or salt SC coefficients to obtain non-negative minimum-area water OH stretch and HOH bend bands. Although the resulting perturbed water bands may not be entirely unique (as they depend on the degree to which pure water and ion SC coefficients are adjusted), the Raman-TLS residual features arising from ion-perturbed shifts in the TBA C-C and C-H bands of interest are quite robust, as long as care is taken to accurately represent the local baseline.

The influence of NaOH and NaI on the solubility of TBA was measured using the following Raman-detected octanolwater phase partitioning strategy. Vials containing 1 mL of aqueous TBA solution with or without the addition of 1 mL of 1-octanol were used to perform Raman measurements of the C-H band area of TBA in the aqueous phase, all obtained under identical conditions. The vials containing two liquid phases were pre-equilibrated for at least 7 days at room temperature (~22 °C). The subsequent Raman measurements were performed after thermally equilibrating the solutions to a temperature of 20.0 °C. The resulting Raman-MCR SC spectra in one- and two-phase solution systems are provided in the Supporting Information (SI). The ratio of the TBA concentration in the aqueous and 1-octanol phase, $P_{w/o}$, was obtained using the following expression, where I_0 and I are TBA CH band areas in aqueous single-phase and two-phase systems, respectively.

$$P_{\text{w/o}} = \frac{[\text{TBA}]_{\text{aq}}}{[\text{TBA}]_{\text{act}}} = \frac{I}{I_{\text{o}} - I}$$

The measured partition coefficient of TBA in the n-octanol/water two-phase system is consistent with the previously reported TBA n-octanol/water $\log P$ values of 0.29 and 0.35, 31,32 corresponding to $P_{\rm w/o}=0.48\pm0.03$, in good agreement with our measured value of $P_{\rm w/o}=0.49\pm0.01$.

Computational EFP-MD Simulations. The three model systems investigated in this study are TBA-water, TBAwater-NaOH, and TBA-water-NaI mixtures, whose representative simulation snapshots are shown in Figure 1. The TBA-water system consists of 4 TBA and 416 water 24 Å³. The water-ion mixtures consist of 4 TBA, 400 water molecules, 8 Na⁺ ions, and 8 negatively charged ions (OH⁻ or I⁻) corresponding to a 0.5 M concentration of TBA and 1.0 M concentration of each ion. Before performing EFP-MD simulations, each system was first equilibrated with classical molecular dynamics (MD) simulations in the GROMACS package (version 2016.5).³³ In these classical simulations, the CHARMM27 force field^{34,35} was used for the TBA molecule, Na⁺ and OH⁻ ions. OPLSAA^{36,37} force field was used for I⁻. Nonbonded force-field parameters for ions are summarized in Table S1. The transferable intermolecular potential with three points (TIP3P) model was used for water.³⁸ After energy minimization, MD equilibrations were performed with NVT ensemble (for 1 ns) and NPT ensemble (for 3 ns). NPT MD simulations were carried out with 2 fs time step with a velocity

rescale thermostat³⁹ for temperature control (300 K) and Parrinello–Rahman barostat⁴⁰ for pressure control (1 bar). C–H and O–H bond lengths were constrained with the LINCS algorithm.⁴¹ A 1 nm cutoff was used to handle Lennard-Jones potentials. Electrostatic long-range interactions were treated with particle mesh Ewald (PME) summations^{42,43} with a real-space cutoff of 1 nm.

Starting from the final atomic configuration of the classical MD simulations, we performed extended molecular dynamics (MD) simulations at the EFP level by representing each molecule as an EFP fragment. The TBA, I-, and Na+ parameters in this study were obtained from previous work.^{29,44} Water parameters are from ref 45. Specifically, TBA and water geometries for EFP parameter computations were optimized with MP2/cc-pVTZ level of theory. The EFP parameters for all molecules were computed with hybrid basis sets, namely, 6-31+G(d)/6-311++G(3df,2p) for TBA, water, and OH^- , 6-311G(d)/6-311++G(3df,2p) for Na^+ , and 6-311G(d)/aug-cc-pVQZ for I⁻. The fragment-fragment electrostatic interactions were damped with the overlap damping functions. 46 Gaussian-type polarization damping was used with POLAB values of 0.1 for anions (OH- and I⁻), 0.6 for water and TBA, and 1.0 for Na⁺ to avoid overpolarization of the system. ⁴⁶ After energy minimization, molecular dynamics (MD) equilibrations were performed with NVT and NPT ensembles for 100 ps each. Then, 900 ps NPT production run was carried out with 2 fs time step at 300 K and 1 bar. All EFP-MD simulations were performed with the EFP-MD module of the LibEFP software library. 47,48 To identify the specific interactions of TBA with solvent, the radial distribution functions g(r) for specific pairs of atoms were computed using EFP-MD trajectories.

■ RESULTS AND DISCUSSION

Figure 2 shows the experimental Raman spectra of water (dashed blue curves) and aqueous solutions containing 0.5 M TBA and either (A) 1 M NaOH or (B) 1 M NaI (black curves). The red and gold curves are the Raman-MCR solutecorrelated (SC) spectra obtained from the aqueous solutions of TBA and either aqueous (A) NaOH or (B) NaI. These SC spectra contain both solute intramolecular vibrational features and features arising from solute-induced perturbations of the vibrational spectrum of water. 24,26-29,49 The SC spectra of TBA (solid red curves) and NaOH (solid gold curves) dissolved in water differ primarily in the hydration-shell O-H stretch band region (at frequencies above 3000 cm⁻¹). Note that the gold NaOH SC spectrum in (A) includes the OHpeak near 3600 cm⁻¹ and broad lower-frequency OH features arising from water molecules surrounding OH⁻, while the gold NaI SC spectrum in (B) consists primarily of a broad peak near 3500 cm $^{-1}$ arising from water molecules hydrogen bonded to I $^{-}$, as previously described. $^{26-29,49}$ The SC spectra of TBA in the aqueous salt solutions (dotted red curves) were obtained by performing a Raman-MCR analysis of the Raman spectra of the salt solution with and without TBA. The Raman spectrum of TBA in pure water (not shown) looks essentially identical to that of TBA in 1 M NaOH, as shown in Figure 2A. The very small difference between the latter spectra is highlighted in the difference between the corresponding SC spectra shown in the inset panel of Figure 2 of TBA in pure water (solid red curve) and in 1 M NaOH (dotted red curve).

The inset panels in Figure 2 show expanded views of the SC spectra of TBA in water (solid red curves) and in the 1 M

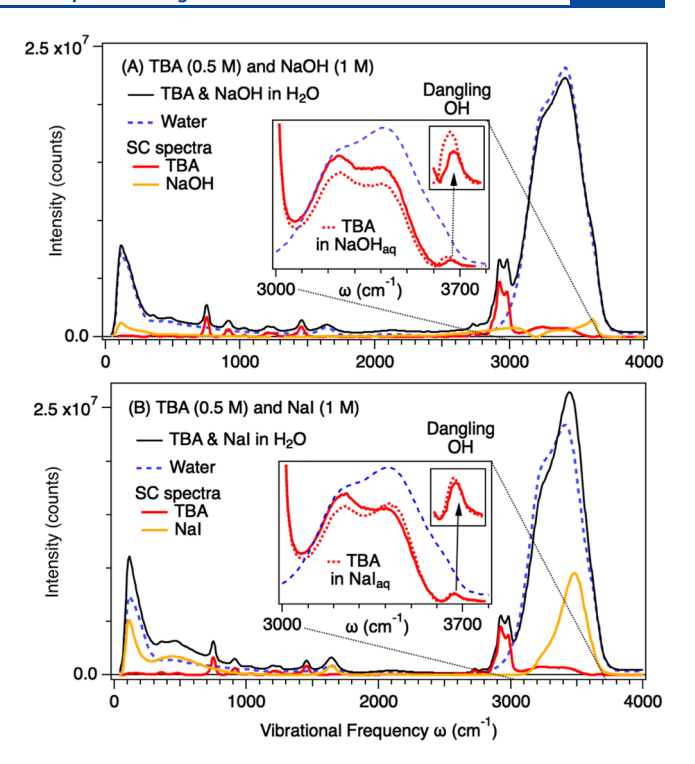


Figure 2. Raman and Raman-MCR spectra of water and aqueous solutions containing 0.5 M TBA and either (A) 1 M NaOH or (B) 1 M NaI. The dashed blue and black curves are the measured Raman spectra of water and TBA in the aqueous ionic solutions, respectively. The red and gold curves are the Raman-MCR SC spectra of TBA in water and the ions in water. The dotted red curves are the SC spectra of TBA in the corresponding aqueous ionic solvent. The inset panels show expanded views of the TBA SC hydration-shell spectra.

aqueous salt solutions (dotted red curves). The difference between the shapes of the solid and dotted red hydration-shell O–H band spectra provides information regarding interactions between the corresponding ions and TBA. Note that NaOH does not significantly change the shape of hydrogen-bonded OH sub-bands peaked near 3200 and 3400 cm⁻¹, while NaI significantly changes the relative areas of these two sub-bands. The decrease in the relative area of the 3200 cm⁻¹ band in NaI is consistent with the penetration of I⁻ into the TBA hydration shell (as previously described), 50 resulting in a decrease in its tetrahedral order relative to TBA in pure water. 51,52 For TBA in NaOH, on the other hand, the similar shape of the two hydrogen-bonded O-H sub-bands implies that NaOH does not significantly change the tetrahedrality of the TBA hydration shell. However, the increased area of the sharper high-frequency OH band area, shown in the small inset panel in Figure 2A, is consistent with the presence of some OHanions that are perturbed by TBA, perhaps in its second hydration shell. The increased area of this high-frequency band also influences the Raman-MCR SC spectral minimization and thus is responsible for the slight decrease in the amplitude of the lower-frequency hydrogen-bonded O-H sub-bands (near 3200 and 3400 cm⁻¹).

Although the above results already imply the greater penetration of NaI than NaOH into the TBA hydration shell, further evidence in support of that conclusion is obtained using a Raman-TLS spectral decomposition strategy. The utility of this strategy derives from the fact that, if there were no interactions between TBA and solvent ions, then one would expect the spectrum of a TBA in an aqueous salt solution to be

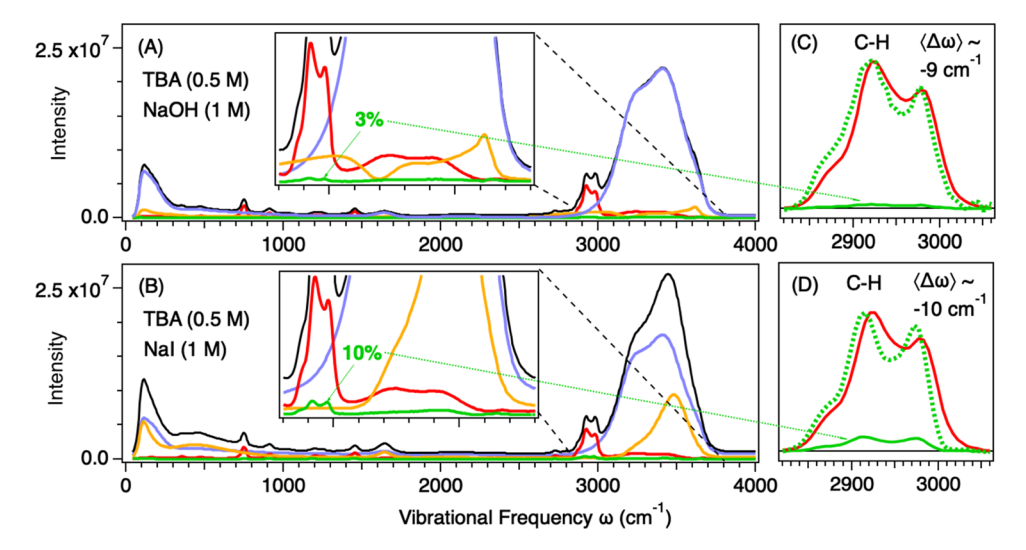


Figure 3. Raman spectra and Raman-TLS decompositions of the spectra of TBA in aqueous (A) NaOH or (B) NaI into a linear combination of pure water (blue curves), SC TBA (red curve), and SC ion component spectra (gold curves). The green spectrum is the minimum-area nonnegative TLS residual containing spectral features resulting from interactions between TBA and the corresponding ions, expanded in (C) and (D), in which the dotted-green curves are scaled to the same peak height as the red CH band of TBA in water.

precisely decomposable into a linear combination of the spectra of pure water, the SC spectrum of TBA in water, and the SC spectrum of the corresponding ions in water. Thus, any vibrational coupling between TBA and the ions would give rise to spectral features in the TLS residual spectrum. Here, we obtain non-negative minimum-area TLS residuals by slightly adjusting the best-fit TLS coefficients to eliminate any negative-going features in the TLS residual (as further described in the Experimental Raman Measurement Methods section).

Figure 3 shows the Raman-TLS decomposition of the Raman spectrum of TBA in aqueous NaOH and NaI solutions (black curves) into a linear combination of the spectra of water (blue curve), SC TBA (red curve), and SC (A) NaOH or (B) NaI (gold curves). The latter aqueous TBA and aqueous salt SC spectra are the same as those shown in Figure 2 (as previously described). 27-29,49,53 What is new here is the nonnegative Raman-TLS residual (green curve), whose low amplitude reflects the relatively small vibrational coupling between TBA and the ions in these solutions. The most obvious difference between the TLS residuals in (A) NaOH and (B) NaI solutions is the appearance of a small C-H band near 2900 cm⁻¹, whose amplitude is about 3% of the full TBA C-H band in NaOH and increases to about 10% in NaI. This increase indicates that more TBA molecules are perturbed by NaI than NaOH and thus provides further evidence that OHis more strongly expelled from the TBA hydration shell than is I-. Note that a previous Raman-MCR study concluded that NaI was mildly expelled from the TBA hydration shell,²⁹ and thus, the present results suggest that OH- is more strongly expelled from the TBA hydration shell than is I⁻. Specifically, the previous study indicating the mild expulsion of I from the hydration shell of TBA²⁹ was performed using Raman-MCR to estimate the number of TBA molecules whose spectra are perturbed by I⁻, thus revealing that the apparent number of TBA-I⁻ contacts was consistent with an association constant of \sim 0.1 M⁻¹, which is significantly smaller than what it would be in a randomly mixture aqueous solution of TBA and NaI. The expulsion of I from the hydration shell of TBA is also reminiscent of the recently reported expulsion of SCN⁻ from

the hydration shell of poly(ethylene oxide) (PEO) monomers, which decreases and then becomes attractive with increasing PEO chain length.⁵⁴

Figure 3C,D contains expanded views of the C-H band of TBA in water (red) and the ion-induced Raman-TLS residual (green) C-H band, scaled to the same peak intensity as the C-H band of TBA in water (dotted green). Comparisons of the latter dotted green and red curves more clearly reveal the red shift and C-H band shape changes induced by NaOH and NaI. The observed red shifts of C-H indicate that ions exert an attractive force pulling out on methyl hydrogens. Our Raman-TLS results further indicated that NaOH exerts a repulsive force along the C-C bond, as evidenced by the blue shift in the C-C band of TBA in aqueous NaOH, and smaller blue shift in aqueous NaI (as shown in the Figure S1, SI).

Further insights regarding the significance of the above experimental Raman-MCR and Raman-TLS results are provided by the following EFP-MD TBA-ion (and TBA—water) distribution function and Kirkwood—Buff predictions. These predictions and comparisons with our Raman-based TBA solubility measurements provide further confirmation that TBA methyl hydration shells more strongly exclude OH⁻ than I⁻ ions, as well as revealing counterion correlations and localizations.

The EFP-MD simulations (discussed in detail in the Computational EFP-MD Simulations section) utilize a quantum-mechanically based potential to describe noncovalent interactions in condensed phase systems. The EFP method represents a molecular system as a collection of rigid fragments that interact with each other through electrostatics, polarization, dispersion, and exchange-repulsion components, all of which are directly derived from first principles. Thus, EFP-MD simulations capture polarization and short-range charge-penetration effects, which have been shown to accurately describe ion solvation. ^{29,44,46} Ion solvation and the thermodynamic properties of ionic solutions and interfaces have also been studied with other polarizable force fields, ^{11,61} as well as force fields including a charge-transfer term or scaled charges.

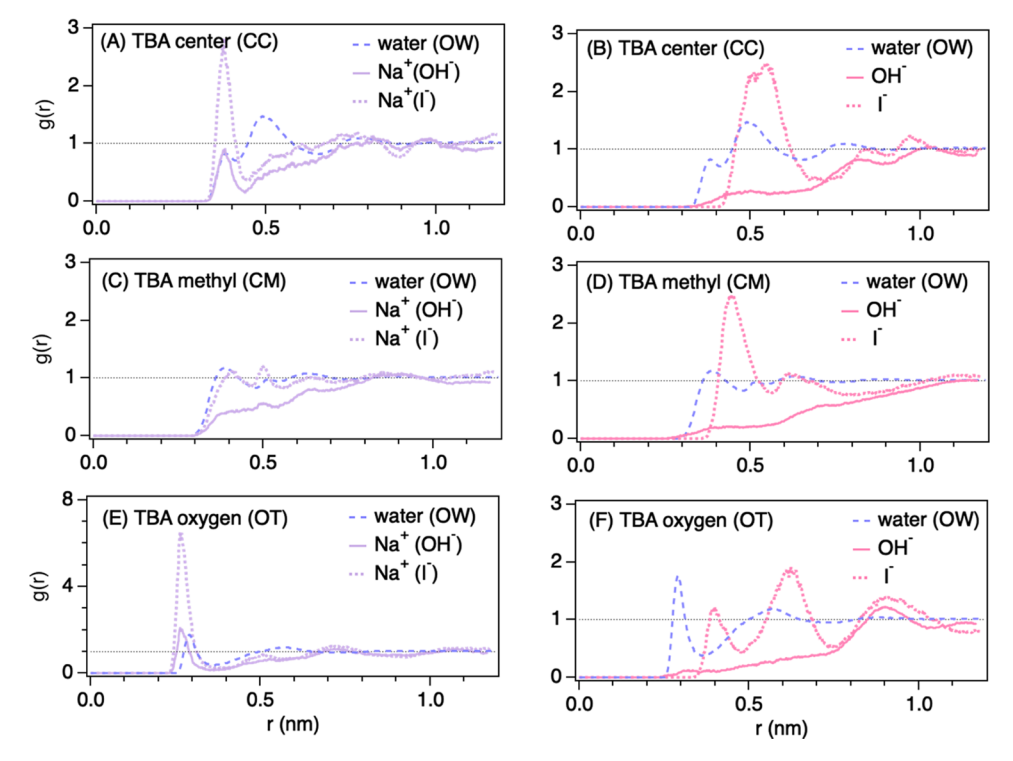


Figure 4. Effective fragment potential molecular dynamics (EFP-MD) predictions of the radial distribution functions of water oxygen (OW), sodium (Na $^+$), hydroxide (OH $^-$), and iodide (I $^-$) about the TBA central carbon (CC), methyl carbon (CM), and hydroxyl head group (OT). The purple (left panels) and salmon (right panels) curves are the cation (Na $^+$) and anion (OH $^-$ or I $^-$) distributions, respectively. The upper, middle, and lower pairs of panels contain distributions relative to TBA CC, CM, and OT atoms, respectively. Note the different vertical axis scale in (E).

Figure 4 compares the predicted radial distribution function g(r) of either water (oxygen atom, OW), Na+, I-, or OH-(oxygen atom) relative to either the TBA central carbon (CC), methyl carbon (CM), or hydroxyl oxygen (OT), obtained from EFP-MD simulations with ~0.5 M TBA in ~1 M aqueous NaI or NaOH. Note that the first two peaks in CC-OW distributions (dashed blue curves in Figure 4A,B) correspond to the hydration shells of the TBA hydroxyl and methyl groups (relative to the TBA central carbon) and thus aid in localizing the corresponding peaks in TBA-ion distributions for Na+ (purple curves) and either OH- or I-(pink curves). The stronger expulsion of OH⁻ than I⁻ from the TBA hydration shell is evidenced by the distributions of these ions about both the central carbon (in Figure 4B) and methyl carbon (in Figure 4D). The corresponding Na⁺ ion distribution (in Figure 4A-D) reveals that Na+ has a significant population near the TBA hydroxyl oxygen (OT), to an extent that is correlated with the affinity of the anion for the methyl hydration shell. Specifically, note that the OT-Na⁺ direct-contact peak (at $r \sim 0.26$ nm) is about 3 times larger for TBA in NaI than in NaOH (Figure 4E). Additionally, comparisons of ion distributions relative to the TBA CC, CM, and OT atoms indicate that the cation and anion have some preference for residing in different parts of the TBA hydration shell, with Na⁺ often located near the TBA hydroxyl head group and both OH⁻ and I⁻ having a slight preference for the hydration shell of the nonpolar (methyl groups) of TBA, although OH⁻ is primarily present in the second hydration shell of TBA. This counterion localization behavior is similar to that recently found for other amphiphilic solutes in aqueous salt solutions.⁶³ Our results further reveal that the local Na⁺ concentration is anion dependent and increases with the affinity of the anion for the TBA methyl groups.

The relative affinities of the NaOH and NaI anions for TBA are consistent with our experimental Raman-TLS results shown in Figure 3. Specifically, EFP-MD results predict that about $\sim\!2\%$ of TBA hydration shells contain OH $^-$ (in 1 M NaOH) and about $\sim\!8\%$ contain I $^-$ (in 1 M NaI), within 4.8 Å of the central carbon of TBA, in quite good agreement with the experimental values of $\sim\!3\%$ and $\sim\!10\%$ inferred from the ion-perturbed C–H band areas shown in Figure 3.

The g(r) results in Figure 4 may also be used to predict salt-induced changes in the solubility and chemical potential of TBA, with the aid of Kirkwood–Buff theory. The resulting solubility predictions, as well as our experimental solubility measurements, definitively confirm that OH^- (and Na^+) are strongly expelled from the TBA hydration shell, thus significantly reducing its solubility, while I^- (and Na^+) is more weakly repelled by TBA, and thus only slightly decreasing its solubility.

Figure 5 shows the Kirkwood–Buff-related predictions obtained from the EFP-MD g(r) results shown in Figure 4. Figure 5A,B contains the Kirkwood–Buff integrands pertaining to water and the two counterions, obtained from the CC–OW and CC-ion g(r) results shown in Figure 4A,B. Figure 5C,D shows the resulting Kirkwood–Buff integrals and TBA chemical potential predictions (obtained using eqs 1–4), where the subscripts A and j pertain to the solute (TBA) and solvent species, respectively, which may be either water (w) or the monovalent cation (s⁺) or anion (s⁻). The influence of a salt of number density ρ_s on the excess chemical potential μ^{\times} and Ostwald solubility λ^{64} of TBA is determined by the corresponding Setschenow (Sechenov) coefficient K_s .

$$G_{Aj}(r) = \int_0^r 4\pi r^2 [g_{Aj}(r) - 1] dr$$
 (1)

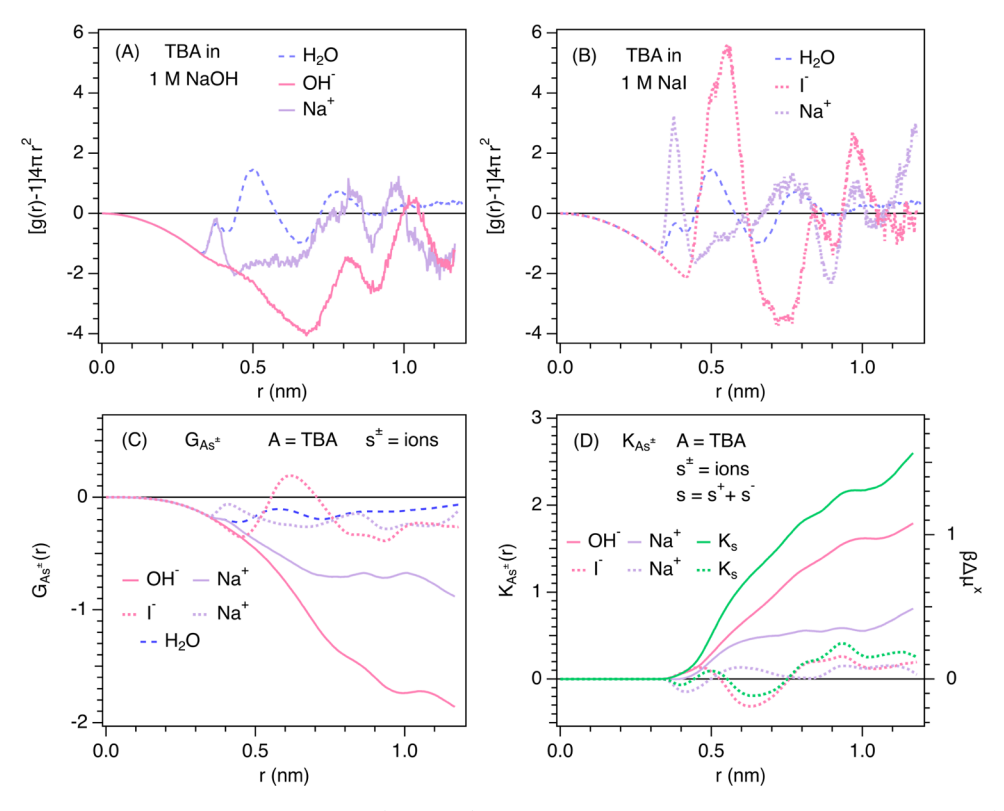


Figure 5. Effective fragment potential molecular dynamics (EFP-MD) predictions of Kirkwood-Buff integrands for TBA in (A) NaOH and (B) NaI, as well as the corresponding (C) $G_{As^{\pm}}$ integrals, and (D) solubility and chemical potential changes $\ln(\lambda/\lambda^{\circ}) = -K_{s}\rho_{s} = -\beta\Delta\mu^{\times}$. The predictions at $r \sim 1$ nm are assumed to approximate the asymptotic values of $G_{As^{\pm}}$ and $K_{As^{\pm}}$. The pink and purple curves pertain to the anion and cation, respectively, and the green curves pertain to the combined influence of both counterions. All predictions are obtained from distributions relative to the central carbon (CC).

$$K_{As^{\pm}}(r) = G_{Aw}(r) - G_{As^{\pm}}(r)$$
 (2)

$$K_s(r) = 2G_{Aw}(r) - G_{As}(r) - G_{As}(r)$$
 (3)

$$\beta \Delta \mu^{\times} = (\mu^{\times} - \mu_{\circ}^{\times})/k_{\rm B}T = \ln(\lambda^{\circ}/\lambda) \approx \rho_{\rm s}K_{\rm s}(r = 1 \text{ nm})$$
(4)

Note that Kirkwood–Buff integrands necessarily have a finite range since $g_{Aj}(r)-1$ must approach zero at large r, although numerical noise in r^2 [$g_{Aj}(r)-1$] at large r can make it difficult to accurately reach this fully converged limit. Thus, although G_{Aj} , $K_{As^{\pm}}$, and K_s should in principle be obtained from the $r\to\infty$ limits of eqs 1 and 2, here we approximate them using the EFP-MD predicted values of $G_{Aj}(r)$ and $K_{As^{\pm}}(r)$ at $r\sim 1$ nm, which upon multiplying by ρ_s yield the predicted salt-induced changes in the TBA excess chemical potential μ^{\times} and solubility λ (where the 0-sub or superscripts pertain to TBA in pure water). The self-consistency of EFP-MD predictions is confirmed by the agreement (to within ± 0.2) between K_s predictions independently obtained from CC, MC, and OT g(r) distribution functions (as shown in the Figure S3, SI).

The results in Figure 5 indicate that in aqueous NaOH, both OH⁻ and Na⁺ are predicted to have negative $G_{\rm As^{\pm}}$ integrals and positive $K_{\rm As^{\pm}}$ coefficients, indicating that these ions are strongly expelled from TBA and decrease its solubility, while in NaI, both $G_{\rm As^{\pm}}$ and $K_{\rm As^{\pm}}$ have smaller magnitudes, thus predicting that the ions are mildly expelled from TBA and only slightly decrease its solubility. These predictions are in good semiquantitative agreement with our experimental TBA solubility measurements, which predict that $\beta\Delta\mu^{\times}=0.69\pm0.04$ ($\lambda^{0}/\lambda\sim2.0$) for TBA in 1 M NaOH and $\beta\Delta\mu^{*}=0.36\pm0.03$

 $0.08 \ (\lambda^0/\lambda \sim 1.4)$ in 1 M NaI. The latter experimental results were obtained by equilibrating TBA in an aqueous/n-octanol two-phase system, with a total TBA concentration of ~0.5 M. The values of λ^0/λ were equated with the measured ratio of the aqueous/n-octanol partition coefficients $(P_{w/o})$ obtained with either pure water or the salt solutions as the aqueous phase (as described in the Experimental Raman Measurement Methods section). The concentration of TBA in the aqueous phase was determined from its C-H band area in the corresponding oneand two-phase systems (as further described in the Experimental Raman Measurement Methods section). Although the experimental $\beta\Delta\mu^{\times}$ value of TBA in 1 M NaOH is about a factor of 2 smaller than the EFP-MD-Kirkwood-Buff predictions of $\beta\Delta\mu^{\times}\sim 1.4$, the experimental and predicted values agree in implying that the solubility of TBA is more significantly decreased (salted-out) by 1 M NaOH than NaI. Moreover, both the predicted and experimental results agree in indicating that $\Delta \mu^{\times} \sim RT \sim$ 2.4 ± 0.7 kJ/mol in NaOH and 0 kJ/mol < $\Delta \mu^{\times}$ < 1 kJ/mol in NaI.

The results in Figure 5C,D further imply that individual cation and anion contributions to $G_{\text{As}^{\pm}}$ and $K_{\text{As}^{\pm}}$ are nearly equivalent to each other in the aqueous NaI solution but are significantly inequivalent in aqueous NaOH solutions in which $G_{\text{As}^{+}} \neq G_{\text{As}^{-}}$ and $K_{\text{As}^{+}} \neq K_{\text{As}^{-}}$ (evaluated at r=1 nm). Although the latter inequivalence clearly violates the Kirkwood–Buff electroneutrality constraint,²⁰ the applicability of this constraint has been questioned by Ben-Naim.²¹ Our additional longer time and larger system size GROMACS-MD simulations suggest that our EFP-MD simulations are reasonably

well equilibrated and approximately system-sized independent (see the Figures S7 and S8, SI). Thus, the lack of local electroneutrality around TBA in NaOH solutions may be a consequence of the first principles-based nonempirical EFP-MD force fields (although it may also be influenced to some degree by the small system size, limited Kirkwood—Buff integration range, and perhaps imperfect equilibration of EFP-MD simulations). This issue, including comparisons with more nearly electroneutral Kirkwood—Buff integral results obtained using GROMACS-MD simulations, is further discussed in the SI (see Figure S9 and the associated text).

SUMMARY AND CONCLUSIONS

Our experimental Raman-MCR and TLS and theoretical EFP-MD simulation results reveal the expulsion OH- from the methyl hydration shells of TBA. The milder expulsion of Ifrom the TBA hydration shell is consistent with that inferred from previous Raman-MCR measurements.²⁹ Our EFP-MD simulations further indicate that the Na+ countercation population is located primarily near the hydroxy head group of TBA, and its hydration-shell concentration is correlated with that of the anion, which is more nearly uniformly distributed around TBA, with an elevated I concentration and depleted OH⁻ near TBA methyl groups. This counterion correlation is similar to that recently inferred from experimental and simulation studies of other amphiphilic solutes in aqueous salt solutions.⁶³ Comparisons of the present results with prior measurements of the solubilities of nonpolar solutes (including H₂, O₂, methane, n-butane, and benzene), ^{16,17,65} as well as recent simulations of methane¹⁹ in various aqueous solutions, confirm that the decreased affinity of anions for nonpolar hydration shells with decreasing anion size also extends to amphiphilic solutes such as TBA. The expulsion of OH⁻ from the three neighboring methyl groups of TBA, combined with the increased air—water surface tensions in aqueous NaOH, 66 and the increase in alkane-water interfacial tension in other salts containing small anions, including NaCl,⁶⁷ suggest that the expulsion of OH⁻ from nonpolar interfaces occurs at both molecular and macroscopic length scales.

ASSOCIATED CONTENT

Supporting Information

The Supporting Information is available free of charge at https://pubs.acs.org/doi/10.1021/acs.jpcb.1c08420.

Additional experimental Raman-TLS, Raman-MCR solubility, EFP-MD, and GROMACS-MD results (PDF)

AUTHOR INFORMATION

Corresponding Author

Dor Ben-Amotz — Department of Chemistry, Purdue University, West Lafayette, Indiana 47907, United States; orcid.org/0000-0003-4683-5401; Email: bendor@purdue.edu

Authors

Aria J. Bredt — Department of Chemistry, Purdue University, West Lafayette, Indiana 47907, United States Yongbin Kim — Department of Chemistry, Purdue University, West Lafayette, Indiana 47907, United States

- Denilson Mendes de Oliveira Department of Chemistry, Purdue University, West Lafayette, Indiana 47907, United States; oorcid.org/0000-0002-2579-8405
- Andres S. Urbina Department of Chemistry, Purdue University, West Lafayette, Indiana 47907, United States; oorcid.org/0000-0001-6482-4736
- Lyudmila V. Slipchenko Department of Chemistry, Purdue University, West Lafayette, Indiana 47907, United States; orcid.org/0000-0002-0445-2990

Complete contact information is available at: https://pubs.acs.org/10.1021/acs.jpcb.1c08420

Notes

The authors declare no competing financial interest.

ACKNOWLEDGMENTS

The work was supported by grants from National Science Foundation (CHE-1763581 for A.J.B., D.M.d.O., A.S.U., and D.B.-A.; and CHE-1800505 for Y.K. and L.V.S.).

REFERENCES

- (1) Creux, P.; Lachaise, J.; Graciaa, A.; Beattie, J. K.; Djerdjev, A. M. Strong Specific Hydroxide Ion Binding at the Pristine Oil/Water and Air/Water Interfaces. *J. Phys. Chem. B* **2009**, *113*, 14146–14150.
- (2) Fang, H.; Wu, W.; Sang, Y.; Chen, S.; Zhu, X.; Zhang, L.; Niu, Y.; Gan, W. Evidence of the Adsorption of Hydroxide Ion at Hexadecane/Water Interface from Second Harmonic Generation Study. *RSC Adv.* **2015**, *5*, 23578–23585.
- (3) Agmon, N.; Bakker, H. J.; Campen, R. K.; Henchman, R. H.; Pohl, P.; Roke, S.; Thamer, M.; Hassanali, A. Protons and Hydroxide Ions in Aqueous Systems. *Chem. Rev.* **2016**, *116*, 7642–7672.
- (4) Uematsu, Y.; Bonthuis, D. J.; Netz, R. R. Impurity Effects at Hydrophobic Surfaces. *Curr. Opin. Electrochem.* **2019**, 13, 166–173.
- (5) Soniat, M.; Kumar, R.; Rick, S. W. Hydrated Proton and Hydroxide Charge Transfer at the Liquid/Vapor Interface of Water. *J. Chem. Phys.* **2015**, *143*, No. 044702.
- (6) Tse, Y.-L. S.; Chen, C.; Lindberg, G. E.; Kumar, R.; Voth, G. A. Propensity of Hydrated Excess Protons and Hydroxide Anions for the Air-Water Interface. *J. Am. Chem. Soc.* **2015**, *137*, 12610–12616.
- (7) Baer, M. D.; Kuo, I. F. W.; Tobias, D. J.; Mundy, C. J. Toward a Unified Picture of the Water Self-Ions at the Air-Water Interface: A Density Functional Theory Perspective. *J. Phys. Chem. B* **2014**, *118*, 8364–8372.
- (8) Vácha, R.; Rick, S. W.; Jungwirth, P.; de Beer, A. G. F.; de Aguiar, H. B.; Samson, J. S.; Roke, S. The Orientation and Charge of Water at the Hydrophobic Oil Droplet-Water Interface. *J. Am. Chem. Soc.* **2011**, *133*, 10204–10210.
- (9) Wick, C. D.; Dang, L. X. The Behavior of NaOH at the Air-Water Interface: A Computational Study. *J. Chem. Phys.* **2010**, *133*, No. 024705.
- (10) Knecht, V.; Levine, Z. A.; Vernier, P. T. Electrophoresis of Neutral Oil in Water. *J. Colloid Interface Sci.* **2010**, 352, 223–231.
- (11) Vácha, R.; Horinek, D.; Berkowitzc, M. L.; Jungwirth, P. Hydronium and Hydroxide at the Interface between Water and Hydrophobic Media. *Phys. Chem. Chem. Phys.* **2008**, *10*, 4975–4980.
- (12) Kudin, K. N.; Car, R. Why Are Water-Hydrophobic Interfaces Charged? J. Am. Chem. Soc. 2008, 130, 3915.
- (13) Zangi, R.; Engberts, J. B. F. N. Physisorption of Hydroxide Ions from Aqueous Solution to a Hydrophobic Surface. *J. Am. Chem. Soc.* **2005**, 127, 2272.
- (14) Pullanchery, S.; Kulik, S.; Okur, H. I.; de Aguiar, H. B.; Roke, S. On the Stability and Necessary Electrophoretic Mobility of Bare Oil Nanodroplets in Water. *J. Chem. Phys.* **2020**, *152*, No. 241104.
- (15) Poli, E.; Jong, K. H.; Hassanali, A. Charge Transfer as a Ubiquitous Mechanism in Determining the Negative Charge at Hydrophobic Interfaces. *Nat. Commun.* **2020**, *11*, No. 901.

- (16) Long, F. A.; McDevit, W. F. Activity Coefficients of Nonelectrolyte Solutes in Aqueous Salt Solutions. *Chem. Rev.* **1952**, *51*, 119–169.
- (17) Weisenberger, S.; Schumpe, A. Estimation of Gas Solubilities in Salt Solutions at Temperatures from 273 K to 363 K. AIChE J. 1996, 42, 298–300.
- (18) Pegram, L. M.; Record, M. T., Jr. Quantifying Accumulation or Exclusion of H(+), HO(-), and Hofmeister Salt Ions near Interfaces. *Chem. Phys. Lett.* **2008**, *467*, 1–8.
- (19) Katsuto, H.; Okamoto, R.; Sumi, T.; Koga, K. Ion Size Dependences of the Salting-out Effect: Reversed Order of Sodium and Lithium Ions. J. Phys. Chem. B 2021, 125, 6296–6305.
- (20) Kusalik, P. G.; Patey, G. N. The Thermodynamic Properties of Electrolyte Solutions: Some Formal Results. *J. Chem. Phys.* **1987**, *86*, 5110–5116.
- (21) Ben-Naim, A. Molecular Theory of Solutions (Section 4.7); Oxford University Press: Oxford, 2006.
- (22) Matt, S. M.; Ben-Amotz, D. Influence of Intermolecular Coupling on the Vibrational Spectrum of Water. *J. Phys. Chem. B* **2018**, *122*, 5375–5380.
- (23) Gierszal, K. P.; Davis, J. G.; Hands, M. D.; Wilcox, D. S.; Slipchenko, L. V.; Ben-Amotz, D. II-Hydrogen Bonding in Liquid Water. J. Phys. Chem. Lett. 2011, 2, 2930–2933.
- (24) Perera, P.; Wyche, M.; Loethen, Y.; Ben-Amotz, D. Solute-Induced Perturbations of Solvent-Shell Molecules Observed Using Multivariate Raman Curve Resolution. *J. Am. Chem. Soc.* **2008**, *130*, 4576–4577.
- (25) Lawton, W. H.; Sylvestre, E. A. Self Modeling Curve Resolution. *Technometrics* 1971, 13, 617–633.
- (26) Ben-Amotz, D. Hydration-Shell Vibrational Spectroscopy. J. Am. Chem. Soc. 2019, 141, 10569–10580.
- (27) Rankin, B. M.; Ben-Amotz, D.; van der Post, S. T.; Bakker, H. J. Contacts between Alcohols in Water Are Random Rather Than Hydrophobic. *J. Phys. Chem. Lett.* **2015**, *6*, 688–692.
- (28) Rankin, B. M.; Hands, M. D.; Wilcox, D. S.; Fega, K. R.; Slipchenko, L. V.; Ben-Amotz, D. Interactions between Halide Anions and a Molecular Hydrophobic Interface. *Faraday Discuss.* **2013**, *160*, 255–270.
- (29) Rankin, B. M.; Ben-Amotz, D. Expulsion of Ions from Hydrophobic Hydration Shells. *J. Am. Chem. Soc.* **2013**, *135*, 8818–8821.
- (30) Bredt, A. J.; Mendes de Oliveira, D.; Urbina, A. S.; Slipchenko, L. V.; Ben-Amotz, D. Hydration and Seamless Integration of Hydrogen Peroxide in Water. *J. Phys. Chem. B* **2021**, *125*, 6986–6993.
- (31) Cumming, H.; Rucker, C. Octanol-Water Partition Coefficient Measurement by a Simple (1)H Nmr Method. ACS Omega 2017, 2, 6244–6249.
- (32) Abraham, M. H.; Chadha, H. S.; Whiting, G. S.; Mitchell, R. C. Hydrogen Bonding. 32. An Analysis of Water-Octanol and Water-Alkane Partitioning and the Delta Log P Parameter of Seiler. *J. Pharm. Sci.* 1994, 83, 1085–1100.
- (33) Abraham, M. J.; Murtola, T.; Schulz, R.; Páll, S.; Smith, J. C.; Hess, B.; Lindahl, E. Gromacs: High Performance Molecular Simulations through Multi-Level Parallelism from Laptops to Supercomputers. *SoftwareX* **2015**, *1*–2, 19–25.
- (34) Foloppe, N.; MacKerell, J.; Alexander, D. All-Atom Empirical Force Field for Nucleic Acids: I. Parameter Optimization Based on Small Molecule and Condensed Phase Macromolecular Target Data. *J. Comput. Chem.* **2000**, *21*, 86–104.
- (35) MacKerell, A. D., Jr.; Banavali, N. K. All-Atom Empirical Force Field for Nucleic Acids: II. Application to Molecular Dynamics Simulations of DNA and Rna in Solution. *J. Comput. Chem.* **2000**, *21*, 105–120.
- (36) Jorgensen, W. L.; Maxwell, D. S.; Tirado-Rives, J. Development and Testing of the OPLS All-Atom Force Field on Conformational Energetics and Properties of Organic Liquids. *J. Am. Chem. Soc.* **1996**, 118, 11225–11236.
- (37) Jorgensen, W. L.; Tirado-Rives, J. The OPLS [Optimized Potentials for Liquid Simulations] Potential Functions for Proteins,

- Energy Minimizations for Crystals of Cyclic Peptides and Crambin. J. Am. Chem. Soc. 1988, 110, 1657–1666.
- (38) Jorgensen, W. L.; Chandrasekhar, J.; Madura, J. D.; Impey, R. W.; Klein, M. L. Comparison of Simple Potential Functions for Simulating Liquid Water. *J. Chem. Phys.* **1983**, *79*, 926–935.
- (39) Bussi, G.; Donadio, D.; Parrinello, M. Canonical Sampling through Velocity Rescaling. *J. Chem. Phys.* **2007**, *126*, No. 014101.
- (40) Parrinello, M.; Rahman, A. Polymorphic Transitions in Single Crystals: A New Molecular Dynamics Method. *J. Appl. Phys.* **1981**, *52*, 7182–7190.
- (41) Mackerell, A. D., Jr.; Feig, M.; Brooks, C. L., III Extending the Treatment of Backbone Energetics in Protein Force Fields: Limitations of Gas-Phase Quantum Mechanics in Reproducing Protein Conformational Distributions in Molecular Dynamics Simulations. J. Comput. Chem. 2004, 25, 1400–1415.
- (42) Darden, T.; York, D.; Pedersen, L. Particle Mesh Ewald: An N-Log (N) Method for Ewald Sums in Large Systems. *J. Chem. Phys.* 1993, 98, 10089–10092.
- (43) Essmann, U.; Perera, L.; Berkowitz, M. L.; Darden, T.; Lee, H.; Pedersen, L. G. A Smooth Particle Mesh Ewald Method. *J. Chem. Phys.* 1995, 103, 8577–8593.
- (44) Hands, M. D.; Slipchenko, L. V. Intermolecular Interactions in Complex Liquids: Effective Fragment Potential Investigation of Water—Tert-Butanol Mixtures. *J. Phys. Chem. B* **2012**, *116*, 2775—2786.
- (45) Flick, J. C.; Kosenkov, D.; Hohenstein, E. G.; Sherrill, C. D.; Slipchenko, L. V. Accurate Prediction of Noncovalent Interaction Energies with the Effective Fragment Potential Method: Comparison of Energy Components to Symmetry-Adapted Perturbation Theory for the S22 Test Set. J. Chem. Theory Comput. 2012, 8, 2835–2843.
- (46) Slipchenko, L. V.; Gordon, M. S. Damping Functions in the Effective Fragment Potential Method. *Mol. Phys.* **2009**, *107*, 999–1016.
- (47) Kaliman, I. A.; Slipchenko, L. V. Libefp: A New Parallel Implementation of the Effective Fragment Potential Method as a Portable Software Library. *J. Comput. Chem.* **2013**, *34*, 2284–2292.
- (48) Kaliman, I. A.; Slipchenko, L. V. Hybrid Mpi/Openmp Parallelization of the Effective Fragment Potential Method in the Libefp Software Library. *J. Comput. Chem.* **2015**, *36*, 129–135.
- (49) de Oliveira, D. M.; Bredt, A. J.; Miller, T. C.; Corcelli, S. A.; Ben-Amotz, D. Spectroscopic and Structural Characterization of Water-Shared Ion-Pairs in Aqueous Sodium and Lithium Hydroxide. *J. Phys. Chem. B* **2021**, *125*, 1439–1446.
- (50) Dinpajooh, M.; Matyushov, D. V. Mobility of Nanometer-Size Solutes in Water Driven by Electric Field. *Phys. A* **2016**, *463*, 366–375.
- (51) Wu, X. E.; Lu, W. J.; Streacker, L. M.; Ashbaugh, H. S.; Ben-Amotz, D. Temperature-Dependent Hydrophobic Crossover Length Scale and Water Tetrahedral Order. *J. Phys. Chem. Lett.* **2018**, *9*, 1012–1017.
- (52) Wu, X. E.; Lu, W. J.; Streacker, L. M.; Ashbaugh, H. S.; Ben-Amotz, D. Methane Hydration-Shell Structure and Fragility. *Angew. Chem., Int. Ed.* **2018**, *57*, 15133–15137.
- (53) Fega, K. R.; Wilcox, D. S.; Ben-Amotz, D. Application of Raman Multivariate Curve Resolution to Solvation-Shell Spectroscopy. *Appl. Spectrosc.* **2012**, *66*, 282–288.
- (54) Rogers, B. A.; Okur, H. I.; Yan, C.; Yang, T.; Heyda, J.; Cremer, P. S. Weakly Hydrated Anions Bind to Polymers but Not Monomers in Aqueous Solutions. *Nat. Chem.* **2021**, DOI: 10.1038/s41557-021-00805-z.
- (55) Hutchinson, E. J.; Ben-Amotz, D. Molecular Force Measurement in Liquids and Solids Using Vibrational Spectroscopy. *J. Phys. Chem. B* **1998**, *102*, 3354–3362.
- (56) Day, P. N.; Jensen, J. H.; Gordon, M. S.; Webb, S. P.; Stevens, W. J.; Krauss, M.; Garmer, D.; Basch, H.; Cohen, D. An Effective Fragment Method for Modeling Solvent Effects in Quantum Mechanical Calculations. *J. Chem. Phys.* **1996**, *105*, 1968–1986.
- (57) Gordon, M. S.; Freitag, M. A.; Bandyopadhyay, P.; Jensen, J. H.; Kairys, V.; Stevens, W. J. The Effective Fragment Potential

- Method: A QM-Based MM Approach to Modeling Environmental Effects in Chemistry. J. Phys. Chem. A 2001, 105, 293-307.
- (58) Gordon, M. S.; Slipchenko, L. V.; Li, H.; Jensen, J. H. The Effective Fragment Potential: A General Method for Predicting Intermolecular Interactions. *Annual Reports in Computational Chemistry*; Elsevier, 2007; Chapter 10, Vol. 3.
- (59) Gordon, M. S.; Smith, Q. A.; Xu, P.; Slipchenko, L. V. Accurate First Principles Model Potentials for Intermolecular Interactions. *Annu. Rev. Phys. Chem.* **2013**, *64*, 553–578.
- (60) Slipchenko, L. V.; Gurunathan, P. K. Effective Fragment Potential Method: Past, Present, and Future. *Fragmentation: Toward Accurate Calculations on Complex Molecular Systems*; John Wiley & Sons, Inc., 2017; pp 183–208.
- (61) Vrbka, L.; Mucha, M.; Minofar, B.; Jungwirth, P.; Brown, E. C.; Tobias, D. J. Propensity of Soft Ions for the Air/Water Interface. *Curr. Opin. Colloid Interface Sci.* **2004**, *9*, 67–73.
- (62) Zeron, I. M.; Abascal, J. L. F.; Vega, C. A Force Field of Li(+), Na(+), K(+), Mg(2+), Ca(2+), Cl(-), and So4 (2-) in Aqueous Solution Based on the Tip4p/2005 Water Model and Scaled Charges for the Ions. J. Chem. Phys. **2019**, 151, No. 134504.
- (63) Drexler, C. I.; Cracchiolo, O. M.; Myers, R. L.; Okur, H. I.; Serrano, A. L.; Corcelli, S. A.; Cremer, P. S. Local Electric Fields in Aqueous Electrolytes. *J. Phys. Chem. B* **2021**, *125*, 8484–8493.
- (64) Ben-Amotz, D.; Raineri, F.; Stell, G. Solvation Thermodynamics: Theory and Applications. *J. Phys. Chem. B* **2005**, *109*, 6866–6878.
- (65) Morrison, T. J.; Billett, F. The Salting-out of Non-Electrolytes. Part II. The Effect of Variation in Non-Electrolyte. *J. Chem. Soc. (Resumed)* **1952**, 3819–3822.
- (66) Weissenborn, P. K.; Pugh, R. J. Surface Tension of Aqueous Solutions of Electrolytes: Relationship with Ion Hydration, Oxygen Solubility, and Bubble Coalescence. *J. Colloid Interface Sci.* **1996**, 184, 550–563.
- (67) Aveyard, R.; Saleem, S. M. Interfacial Tensions at Alkane-Aqueous Electrolyte Interfaces. *J. Chem. Soc., Faraday Trans.* 1 1976, 72, 1609–1617.